JOURNAL OF MATERIALS EDUCATION (Electronic)

Original Research

# Reading Motion in Polarized Polymer Electrolytes: Heterodyne XPCS with Explicit Acquisition-Time Alignment

Waqas Hamid[1], Ashiq Ali[2,*], Muhammad Kashif[2], Kamran Hanif[2]

[1]*Government College University, Lahore Pakistan*
[2]*The University of Lahore, Pakistan*

**Correspondence to:**
arhamus-man2001@gmail.com

**RECEIVED:**
19/02/2026
**ACCEPTED:**
03/10/2026
**AVAILABLE ONLINE:**
31/10/2026

## ABSTRACT

Spatially resolved operando measurements combine information about material motion with the acquisition schedule used to observe it. This study examines that coupling in heterodyne X-ray photon correlation spectroscopy of polarized polystyrene-block-poly(ethylene oxide)/LiTFSI electrolytes. The analysis concerns fitted speed magnitudes at five nominal positions in three cells, with electrochemical records defining the electrical transitions. A coherent-field derivation establishes why an intensity correlation cannot distinguish opposite directions of translation. A time-alignment calculation then separates a connected sequence of observations from an estimated simultaneous profile. Of 426 measurement rows, 400 contain finite fitted records; 48 complete profiles satisfy phase-preserving interpolation rules. The five-position timestamp span is approximately 25 minutes. Median root-mean-square alignment adjustments are 0.0139, 0.0251 and 0.0464 nm s$^{-1}$ for cells N, O and P. The largest individual adjustment is 0.320 nm s$^{-1}$. Spatial slope signs change in four retained profiles from P, without implying reversal of the polymer velocity. Comparisons with monotone cubic interpolation, stricter temporal bracketing and exclusion near electrical transitions delimit these observations. The study connects interference physics, electrical timing, spatial registration and the interpretation of fitted quantities through numerical examples and measurement-based figures. Its central educational task is to identify which physical conclusions the recorded observable can support.

## KEYWORDS

heterodyne XPCS; polymer electrolyte; operando scattering; temporal alignment; spatial registration; materials characterization

© 2026 The Authors

This is an open access article published by InterPore under the terms of the Creative Commons Attribution-NonCommercial-NoDerivatives 4.0 International License (CC BY-NC-ND 4.0) (https://creativecommons.org/licenses/by-nc-nd/4.0/).

## 1. INTRODUCTION

A spatial profile is more than an ordered collection of values. It asserts that positions can be compared at an adequately specified material state. This assertion becomes consequential when a characterization instrument visits positions sequentially while an electrochemical cell continues to evolve. A concentration gradient develops, interfaces respond, local stresses change, and scattering domains may move during the interval needed to complete the scan. Drawing a line through the measurements does not remove those changes. The horizontal coordinate describes location, but each point also carries an observation time. Understanding how the two coordinates enter the physical interpretation is a necessary part of learning an operando technique.

Polymer electrolytes make this issue particularly instructive because their conducting and mechanically supporting components can occupy different environments. Ion diffusion and migration depend on local interactions and collective correlations, rather than on a single mobility assigned independently of composition [1]. In block copolymers, defects in the nanostructure influence transport, while complete electrochemical characterization can distinguish materials with different morphologies [2, 3]. Salt also affects the phase behavior of the host [4]. Consequently, a local scattering signal cannot automatically be interpreted as a direct measurement of ionic conductivity. The physical origin of its contrast must be established before its time dependence is assigned to a transport process.

Electrical polarization complicates that assignment. Time-dependent structural changes in a block copolymer electrolyte and orientation-dependent distortions of lamellae under direct-current polarization demonstrate that a working material can depart from its equilibrated structure [5, 6]. Limiting-current behavior likewise depends on nanostructure, and a polarization-induced transition can be inaccessible even when it occurs in equilibrated material [7, 8]. These observations motivate measurements during operation. They also explain why an acquisition lasting several minutes can be sensitive to the path taken through electrical and structural states. The study therefore treats time registration as part of the measurement, rather than as a cosmetic step performed after plotting.

Transport interpretation additionally depends on the reference frame. Negative Stefan–Maxwell coefficients in polymer electrolytes, reference-frame transformations of transference numbers, and the contribution of solvent motion illustrate that apparently similar transport quantities can carry different definitions [9–11]. Electrophoretic nuclear magnetic resonance can determine species velocities, whereas local volume conservation constrains how measured motion relates to charge transport [12, 13]. Spatially resolved concentration and velocity measurements provide complementary information [14]. A scattering-derived speed can therefore inform electrolyte physics without being equivalent to an ion velocity, a transference number or a complete transport characterization.

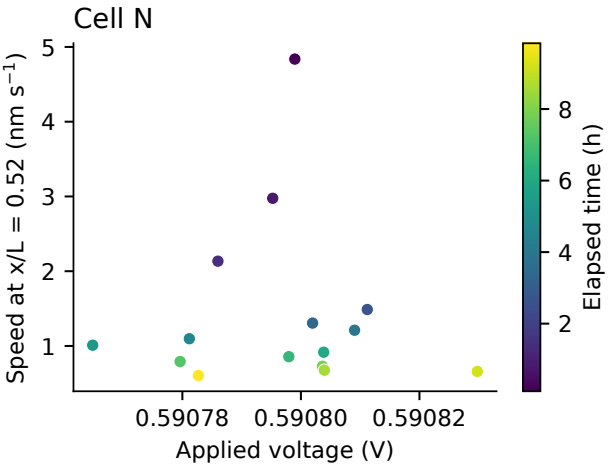
Operando heterodyne X-ray photon correlation spectroscopy, abbreviated XPCS, offers a route to exceptionally slow motion inside an electrolyte. A stationary scattering contribution mixes coherently with a dynamic contribution, allowing relative phase evolution to generate an oscillatory term in the intensity correlation. Concentration and velocity profiles have been measured in a polymeric lithium-ion electrolyte, and the approach has been applied to a microphase-separated block copolymer [15, 16]. The latter experiment supplies the fitted quantities examined here. Its scientific purpose concerns transport under polarization; the present study asks a different question about those quantities: how strongly does their apparent spatial arrangement depend on the time assigned to each observation?

The technique sits within a rapidly developing characterization landscape. Coherent X-ray heterodyning has enabled velocity measurements in flowing materials, and heterodyne signals can also reveal motion in amorphous ice [17, 18]. General XPCS methods connect scattering contrast, coherence and dynamic structure [19]. More recent polymer measurements combine small-angle XPCS with wide-angle scattering to relate dynamics and structure [20]. These advances make it increasingly important to teach the distinction between an observable, the function fitted to it, and the physical quantity inferred from that fit. A convincing fit is necessary for many interpretations, but it is not sufficient to establish a uniquely identifiable direction or a simultaneous spatial field.

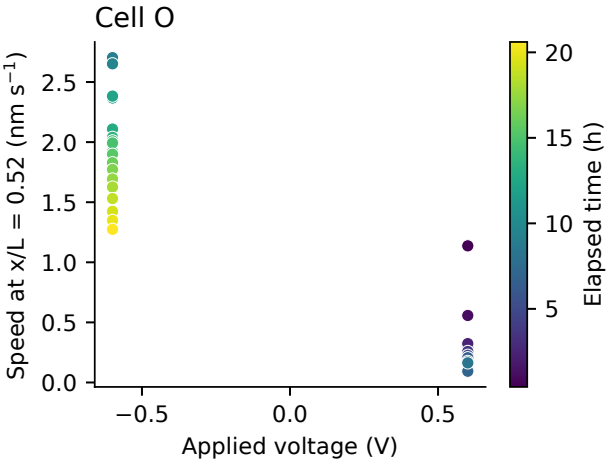
There are two distinct time coordinates in this problem. Correlation delay compares scattering intensities separated within an acquisition. Electrochemical elapsed time locates that acquisition within the operating history of the cell. Confusing these coordinates can lead to a second confusion between changes within a measurement and changes between measurements. Two-time correlation analysis explicitly addresses non-equilibrium evolution, and its interpretation differs from a one-time correlation formed by averaging over an entire observation interval [21, 22].

The instructional contribution is a worked connection between interference symmetry, clock conversion, protocol-aware interpolation and spatial interpretation. The derivation explains why opposite projected velocities yield the same oscillatory intensity term. The calculation identifies which five-position scans can be estimated at a common reference time without extrapolation or interpolation through an electrical transition. Further checks assess alternative interpolation, interval restrictions and fit-parameter variation. Every graphical comparison uses the recorded measurements or quantities calculated from them.

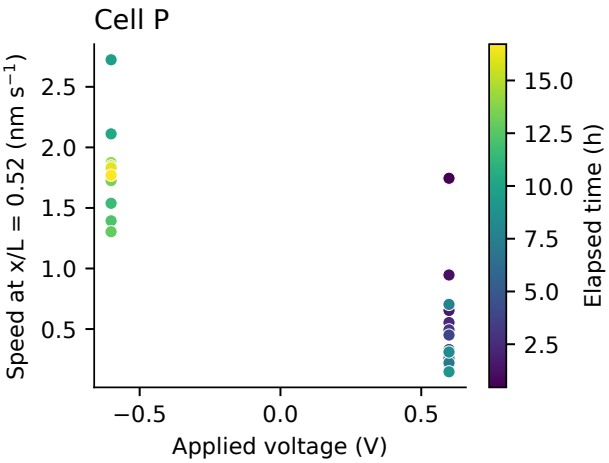
The scope is a specialized study on a contemporary operando application. General XPCS is established, and this article does not assert that the technique is absent from every textbook. The contribution instead rests on its explicit educational question and transparent numerical treatment. It is intended for readers familiar with scattering vectors, elementary electrochemistry and interpolation who need to learn how acquisition history constrains the meaning of a material property map.




(a) Cell N




(b) Cell O




(c) Cell P

**Figure 1:** Electrical state and fitted speed at the fourth nominal position. Color indicates elapsed time during the recorded chronoamperometry interval. Points outside that interval are omitted from this voltage comparison. Nonnegative speed values after a polarity change reflect the fitted magnitude; they do not establish the direction of polymer motion.

# 2. OBSERVABLE, INTERFERENCE AND DIRECTIONAL IDENTIFIABILITY

## 2.1. What the scattering contrast follows

The material considered is a polystyrene-block-poly(ethylene oxide) electrolyte containing lithium bis(trifluoromethanesulfonyl)imide, denoted SEO/LiTFSI. The polystyrene and poly(ethylene oxide) blocks have molar masses of 19 and 20 kg mol$^{-1}$, respectively, and the ratio of lithium salt to ethylene oxide units is 0.08. Measurements were performed at 90 °C in a lithium symmetric-cell geometry with a 3 mm electrode separation. The beam traversed the electrolyte parallel to the electrodes, and a separate unpolarized compartment supplied reference scattering [16]. These conditions specify the physical system; they do not establish that all dynamical contributions can be represented by a single moving species.

At the scattering angles used in the experiment, contrast is associated with the microphase-separated polymer structure. Salt partitions predominantly into the conducting environment, but the scattering domains are not individual lithium ions. The fitted motion therefore describes the scattering structure under the adopted model. This distinction matters when interpreting Figure 1: measured speeds remain nonnegative when the applied voltage changes sign. The plot does not show that the direction stays unchanged. It shows that the observable supplied to the analysis is a magnitude and that electrical polarity and fitted speed are different quantities.

Independent concentration measurements provide a different constraint on the cell. X-ray absorption can be related to salt concentration for a binary electrolyte, while operando scattering accesses structural or dynamical information [23, 24]. Neither signal substitutes automatically for the other. A local domain speed without composition, constitutive relations and boundary conditions cannot determine the complete set of frictional interactions. Likewise, a concentration profile alone does not identify which material component produces a coherent scattering signal. The strength of combining measurements lies in preserving their distinct physical sensitivities.

## 2.2. Why the intensity correlation loses the sign

Let the detector receive a stationary reference field $E_r(\mathbf{q})$ and a time-dependent field $E_d(\mathbf{q}, t)$. Their coherent sum produces

$$I(\mathbf{q}, t) = |E_r + E_d|^2 = |E_r|^2 + |E_d|^2 + 2\,\mathrm{Re}(E_r^* E_d). \tag{1}$$

The interference term carries relative phase. For a translating scattering structure, a displacement $\mathbf{v}\tau$ over correlation delay $\tau$ introduces a phase increment $\mathbf{q} \cdot \mathbf{v}\tau$. A motion-dependent contribution to the intensity correlation can therefore be represented by

$$H(\mathbf{q}, \tau) = A(\mathbf{q}, \tau) \cos(\mathbf{q} \cdot \mathbf{v}\tau), \tag{2}$$

where $A$ contains the decaying envelope and other multiplicative factors. Eq. (2) isolates the directional argument; the full fit also includes contrast, mixing fraction and decorrelation contributions. It should not be substituted for the complete fit when estimating parameters from detector intensities.

Because the cosine is even, reversal of the projected motion leaves this term unchanged:

$$H(\mathbf{q}, \tau; \mathbf{v}) = H(\mathbf{q}, \tau; -\mathbf{v}). \tag{3}$$

This equality is an identifiability statement. It persists even for perfectly precise intensities and an arbitrarily successful fit. Reducing random noise cannot remove a symmetry of the measurement function. Direction can be assigned only through an additional observation or a physical argument whose assumptions are stated separately. In particular, multiplying every speed after a voltage reversal by a negative sign would create a model-based signed quantity, not reveal a sign directly contained in the fitted table.

Dimensional analysis is equally important. If $q$ is in $\mathrm{nm}^{-1}$, speed is in $\mathrm{nm\,s}^{-1}$ and delay is in seconds, the phase argument is dimensionless. Angular frequency is $\omega = \mathbf{q} \cdot \mathbf{v}$, whereas the period is $2\pi/|\omega|$. For a projected speed of $1\ \mathrm{nm\,s}^{-1}$ and $q = 0.16\ \mathrm{nm}^{-1}$, the corresponding period is 39.3 s. This numerical example checks units; it is not a fit to a measured correlation. Omitting the factor $2\pi$ would change the inferred speed even though the plotted oscillation remained visually plausible.

## 2.3. Three temporal scales that must remain separate

An individual acquisition recorded patterns every 60 ms for 360 s, yielding 6000 frames. This frame interval sets one temporal sampling scale. The acquisition duration sets another because a fitted parameter summarizes the scattering during that window. A third scale is the interval between visits to different positions or repeated visits to the same nominal position. Faster detectors, including high-throughput microsecond acquisitions and nanofocused XPCS, expand the accessible dynamical range but do not by themselves make a spatial scan simultaneous [25, 26].

Coherent sources also permit measurements over very different delay ranges, from rapid molecular motion to slow relaxation [27–29]. These capabilities should not be conflated with the temporal resolution of a complete operando map. A detector may resolve short delays while the mechanical or statistical requirements of the spatial acquisition impose a much longer map interval. The study concerns that latter interval and the interpretation of fitted values assigned to it. It makes no claim to recover motion within an individual 360 s window from a single tabulated speed.

# 3. MEASUREMENTS AND NUMERICAL TREATMENT

## 3.1. Experimental Measurements and Quantitative Analysis

Dynamic processes in materials using experimental measurements and quantitative analysis to characterize their temporal behavior is examined [16, 30]. The investigation examined fitted speed magnitudes and corresponding timing information, providing insights into the evolution of the observed processes under the experimental conditions. The relationship between measured velocities and temporal variations offers a basis for understanding the dynamics of the investigated system and interpreting its physical behavior. These findings provide a foundation for subsequent numerical comparisons, evaluation of temporal trends, and quantitative interpretation of experimental observations. The measurements also support educational applications involving the analysis of material dynamics, the interpretation of experimental results, and the relationship between measurable physical quantities and underlying material behavior.

Three cell labels, N, O and P, distinguish the measurement series. Each fitted record can contain a speed, acquisition timestamp, nominal position, contrast-related parameters and motor coordinates. Electrochemical records contain time and applied voltage. The available numerical material comprises 426 rows, of which 400 have finite speed, timestamp and nominal-position entries. There are three cell-level series, not 400 independently prepared specimens. Positions and times within a cell are repeated observations, and the records do not establish independence of preparation batches. The analysis is accordingly descriptive and deterministic rather than a population hypothesis test.

The speed column is expressed in angstroms per second, as indicated by the accompanying plotting instructions. Multiplication by 0.1 converts it to $\mathrm{nm\,s^{-1}}$. Nominal positions one through five correspond to $\xi = x/L = 0.22, 0.32, 0.42, 0.52, 0.62$. These normalized coordinates are taken from the documented position mapping. They are not recalculated from motor coordinates without an independently established electrode registration. Table 1 distinguishes row completeness, scan identities and eligibility for temporal alignment.

**Table 1:** Measurement accounting and temporal support.

| Cell | Rows | Finite records | Missing rows | Attempted prefixes | Finite prefixes | Complete profiles | Retained profiles |
|---|---|---|---|---|---|---|---|
| N | 106 | 101 | 5 | 22 | 22 | 18 | 13 |
| O | 180 | 168 | 12 | 36 | 36 | 25 | 19 |
| P | 140 | 131 | 9 | 30 | 29 | 21 | 16 |
| Total | 426 | 400 | 26 | 88 | 87 | 64 | 48 |

## 3.2. Clock alignment and electrical phases

The XPCS and electrochemical timestamps use different numerical origins. With the documented constant offset, electrochemical elapsed time in hours is calculated as

$$t = \frac{e_X + 631134000 - e_{0,c}}{3600}, \tag{4}$$

where $e_X$ is the recorded XPCS time in seconds. The electrochemical onset origins $e_{0,c}$ are 1603334515, 1603400605 and 1603498690 s for N, O and P. Electrochemical epoch values are stored in nanoseconds and are divided by $10^9$ before subtraction. These constants are necessary to reconstruct the relative timing; calendar dates and transfer details have no role in the physical interpretation.

For O and P, the polarity boundary is defined by the first negative-voltage row in the chronoamperometry record. The resulting transition times are 8.8611 and 9.1500 h. For N, the end of polarization is approximated by the last chronoamperometry time plus the 5 s electrical sampling interval, giving 10.0486 h. These definitions use electrical observations rather than rounded values inferred from a graph. They are operational boundaries with the precision of the records, not a certification of the absolute accuracy of the two clocks.

A phase label distinguishes observations before onset, during the first polarization and after reversal or cessation. Interpolation through any defined electrical boundary is disallowed. A further conservative check rejects a profile if either endpoint of any interpolation bracket lies within 0.1 h of onset or the transition. This six-minute clearance matches one acquisition duration, but it cannot resolve an unspecified timestamp convention. It tests whether conclusions depend strongly on observations immediately adjacent to a known electrical change.

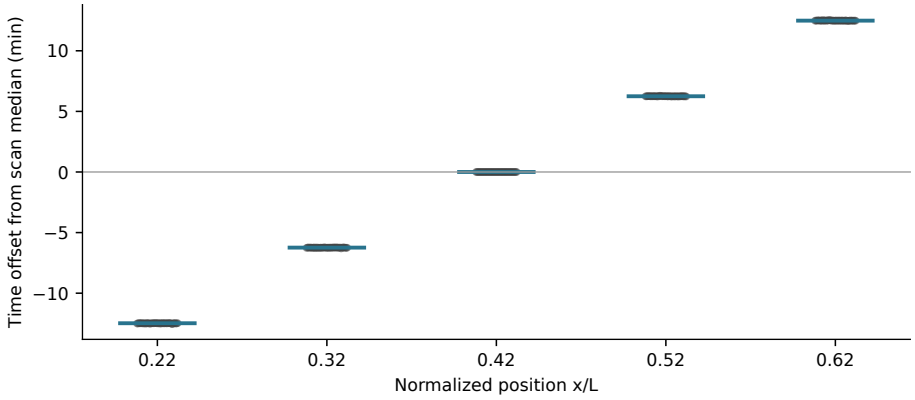



**Figure 2:** Observation-time displacement within all retained five-position scans. Each point gives the difference between its stored timestamp and the median timestamp of that scan; short horizontal marks indicate position-specific medians. The central visit is unchanged by construction. The consistent early-to-late ordering couples observation time to nominal position.

## 3.3. Scan eligibility and a common reference time

A scan identity is obtained from the common prefix of its measurement identifiers. Candidate profiles must contain exactly one finite record at each of the five nominal positions. A prefix with no finite point still belongs in the acquisition accounting, although it cannot supply a profile. This distinction produces 88 attempted scan prefixes and 87 prefixes represented among the finite records. The difference is confined to P and prevents silent removal of a completely unusable attempt from the denominator.

For complete scan $k$, the target time $t_k^*$ is the median of its five recorded times. Using the median keeps the reference inside the observation sequence and makes the central visit an actual observation at the target. Figure 2 shows the relative timing at each nominal position. The construction does not presume that all five values describe an instantaneous state. It defines a time at which a simultaneous comparison will be estimated, subject to explicit temporal support at every position.

At position $i$, let the nearest observations bracketing $t_k^*$ be $(t_a, u_a)$ and $(t_b, u_b)$. The linear estimate is

$$\widehat{u}_i(t_k^*) = u_a + \frac{u_b - u_a}{t_b - t_a}(t_k^* - t_a). \tag{5}$$

An exact observation at the target is retained unchanged. Extrapolation is prohibited, and both bracket endpoints must lie in the target electrical phase. The main calculation imposes $t_b - t_a \le 1.5$ h. If any of the five positions fails a rule, the entire profile is excluded. This whole-profile rule avoids comparing spatial shapes assembled from different numbers of available positions.

The interval ceiling is an analysis choice, not a relaxation time of the material. Its effect is examined at 0.75, 1.0 and 2.0 h. A shorter ceiling reduces exposure to unsupported interpolation but can preferentially remove periods with missing observations. Consequently, eligibility and adjustment magnitude must be considered together. Figure 3

provides the first-failing-reason accounting, and Figure 4 examines the fraction of complete scans retained as the ceiling changes.

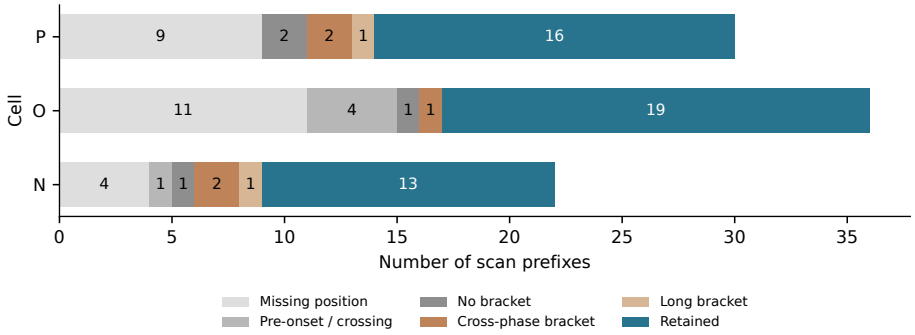



**Figure 3:** Accounting of attempted scan prefixes by the first failed eligibility condition. The retained category satisfies complete position coverage, temporal bracketing, phase preservation and the 1.5 h interval ceiling. Counts include the P prefix with no finite observation. Categories describe the implemented decision order, not mutually independent causes of missing fits.

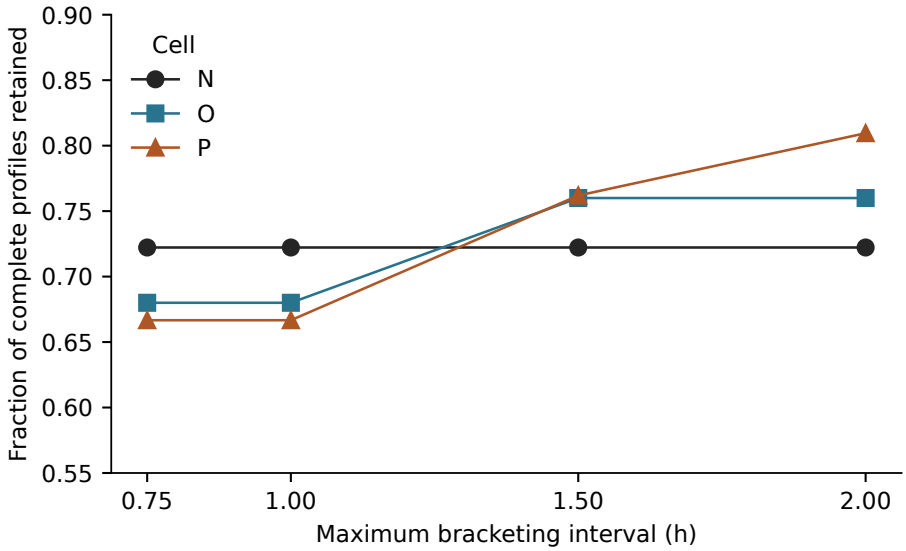



**Figure 4:** Temporal-support requirements change which complete spatial scans enter the comparison. The ordinate divides retained scans by the complete-profile counts of 18, 25 and 21 in N, O and P. Values for a scan retained at several ceilings are identical under linear interpolation; changes in aggregate summaries therefore reflect selection.

## 3.4. Adjustment magnitude, spatial slope and interpolation shape

For each retained position, the alignment adjustment compares the common-time estimate with the sequentially acquired value:

$$\delta_{ki} = \widehat{u}_i(t_k^*) - u(x_i, t_{ki}), \qquad D_k = \left( \frac{1}{5} \sum_{i=1}^{5} \delta_{ki}^2 \right)^{1/2}. \tag{6}$$

Here $D_k$ is a root-mean-square change in $\mathrm{nm\,s^{-1}}$. It is neither a fit uncertainty nor an error relative to an independently measured simultaneous profile. The maximum absolute point adjustment is retained as a separate quantity. Figure 5 preserves the sign of the adjustments, which a scalar root-mean-square value necessarily discards.

An ordinary least-squares line through speed versus $\xi$ supplies a compact spatial trend. Its slope is

$$b_k = \frac{\sum_i (\xi_i - \overline{\xi})(u_{ki} - \overline{u}_k)}{\sum_i (\xi_i - \overline{\xi})^2}. \tag{7}$$

The same expression is applied to aligned values. Its units are $\mathrm{nm\,s^{-1}}$ per unit normalized position. A slope sign change concerns the spatial variation of speed magnitude; it does not determine the direction of translation. Curved profiles can also have small overall slopes, so this diagnostic is not treated as a complete description of spatial structure.

A shape-preserving piecewise cubic Hermite interpolator provides a second estimate at the same target times. It uses observations at the same nominal position within the same electrical phase, while the linear eligibility rules remain fixed. Its local shape depends on neighboring slopes as well as the bracketing values. Comparing the two estimates probes interpolation dependence without presenting either as the true field. The comparison is especially useful near rapid changes where a straight segment and a curved trajectory can pass through the same observations yet differ at the target time.

# 4. RESULTS AND DISCUSSION

## 4.1. Completeness is not equivalent to temporal support

The row accounting gives 101 finite records from 106 rows in N, 168 from 180 in O, and 131 from 140 in P. Their scan prefixes number 22, 36 and 30 before removal of nonfinite entries. Complete five-position profiles number 18, 25 and 21. The main temporal rules retain 13, 19 and 16, respectively. Thus, only 48 of 64 complete scans support the specified aligned comparison. The difference is important: a visually complete spatial curve can still require extrapolation or an interpolation through a change in electrical state.

The exclusions are mutually assigned in the order of checking. N has four incomplete scans, one pre-onset or crossing scan, one without a bracket, two with a bracket crossing a phase boundary, and one exceeding the interval ceiling. O has eleven incomplete scans, four pre-onset or crossing scans, one without a bracket and one crossing a phase boundary. P has nine incomplete scans, two without a bracket, two crossing a boundary and one exceeding the ceiling. Figure 3 presents these counts without treating a missing fit as zero speed.

This first-failure convention prevents double counting but should not be mistaken for a unique physical diagnosis of a rejected scan. A scan rejected for one reason could fail another condition that is never reached. The counts describe the implemented decision sequence. They show that incompleteness and phase-aware temporal support both matter, while leaving the causes of missing fits unresolved. Inferring detector failure, irreversible sample damage or a specific material instability from an empty row would require information not contained in the fitted table.

The three cells should also remain distinct in interpretation. Their electrical histories and fitted-parameter treatment are not identical, and their records do not provide a matched replication design. Pooling every finite point would give O greater weight simply because it contains more observations. The comparisons instead retain cell labels and use counts appropriate to each calculation. This preserves the educational lesson about repeated observation without creating a precision claim based on an inflated number of independent samples.

## 4.2. The spatial sequence extends over twenty-five minutes

The median first-to-last timestamp spans are 24.987, 24.983 and 24.973 min for the retained profiles of N, O and P. Across the retained set, spans range from 24.932 to 25.057 min. Relative to the scan median, the first and last nominal positions lie approximately twelve and a half minutes earlier and later. The second and fourth lie approximately six and a quarter minutes away. These offsets are visible in Figure 2; they reflect a persistent acquisition order rather than random timing variation.

The span is distinct from the duration of a complete scan including the last observation window. Each fitted value summarizes a 360 s acquisition, whereas the approximately 25 min quantity is the difference between recorded reference timestamps at the first and last positions. Without knowing whether those timestamps mark a start, midpoint or another acquisition reference, adding or subtracting a half-window would introduce an undocumented

assumption. The analysis therefore keeps the stored convention and describes the span precisely as a timestamp difference.

The effect on a profile depends on how speed changes during that interval. For a locally smooth field, expansion about the common time gives

$$u(x_i, t_{ki}) \simeq u(x_i, t_k^*) + \left.\frac{\partial u}{\partial t}\right|_{x_i, t_k^*} (t_{ki} - t_k^*). \tag{8}$$

A consistent scan order couples the temporal term to position. If speed decreases during acquisition, late positions may appear lower even when the simultaneous spatial variation is weaker. If it increases, the ordering can act in the opposite direction. This explains why a timing correction can alter a spatial slope without any error in the individual fitted numbers.

The expression is a local explanation, not the numerical estimator. Eq. (5) is used for the main calculation, and it relies on actual repeated observations at each nominal position. Eq. (8) clarifies which physical assumption would make sequential and simultaneous profiles approximately equivalent: temporal changes over the scan must be negligible compared with the spatial contrast under discussion. That assumption should be assessed for the material state, rather than inherited from a plotting convention.

## 4.3. Alignment adjustments are localized and signed

Median root-mean-square changes are 0.01394, 0.02514 and 0.04640 nm s$^{-1}$ for N, O and P. The corresponding maxima are 0.03319, 0.20207 and 0.18436 nm s$^{-1}$. Table 2 retains both summaries because a median alone would obscure the larger changes in a small part of the record. Their cross-cell differences do not establish that one material is more temporally unstable: acquisition availability, electrical history and fitting choices also differ.

The adjustment matrices in Figure 5 show why sign matters. The central nominal position remains unchanged because its timestamp equals the selected median. Earlier and later visits can require adjustments in opposite directions, even within one scan. A large root-mean-square change can therefore be associated with a reshaping of the profile, rather than a uniform vertical displacement. Conversely, a small aggregate value can coexist with one position that is influential for a particular local comparison.

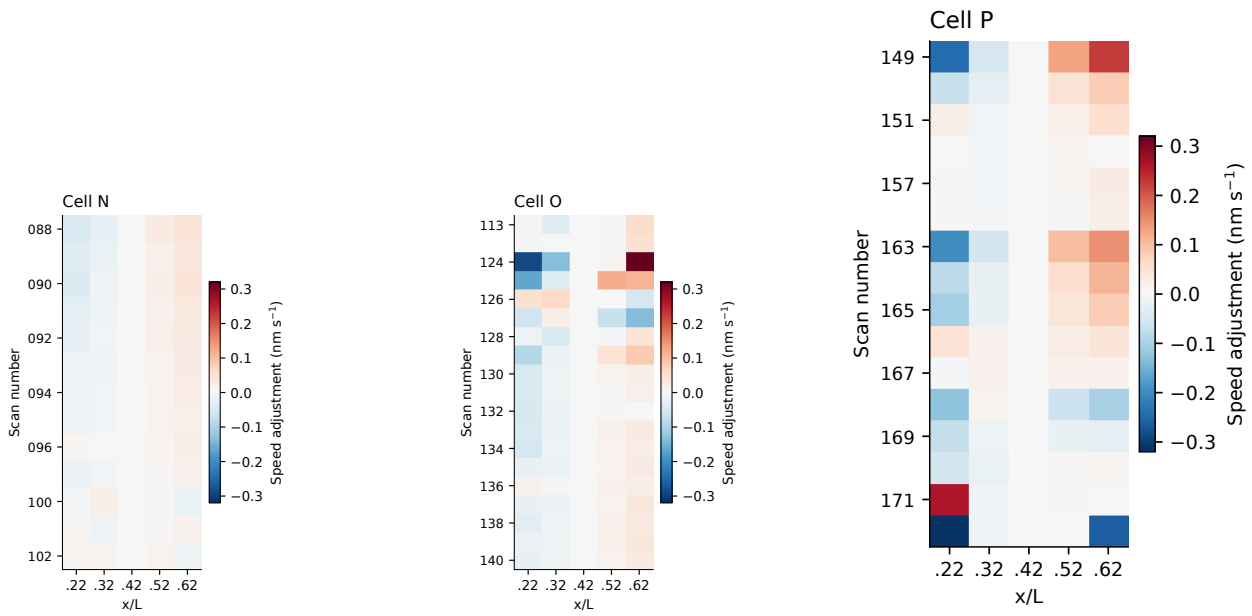
**Table 2:** Alignment adjustments under the 1.5 h bracket rule. All speed quantities are in nm s$^{-1}$.

| Cell | Median $D$ | Maximum $D$ | Cubic median $D$ | Cubic maximum $D$ | Slope changes |
|---|---|---|---|---|---|
| N | 0.01394 | 0.03319 | 0.01328 | 0.03392 | 0/13 |
| O | 0.02514 | 0.20207 | 0.02388 | 0.19703 | 0/19 |
| P | 0.04640 | 0.18436 | 0.04939 | 0.17165 | 4/16 |

The largest individual adjustment occurs in O124 at $\xi = 0.62$. Its recorded speed is 2.21044 nm s$^{-1}$, acquired 12.488 min after the target. Linear interpolation estimates 2.53030 nm s$^{-1}$ at the scan reference of 9.44208 h, producing an increase of 0.31986 nm s$^{-1}$. Figure 6 displays the temporal support for this estimate. It places the interpolation in time rather than drawing another spatial profile, making the actual observations and the estimated target value visually distinguishable.

The first position of the same scan is observed 12.517 min before the target. Its value of 3.51154 nm s$^{-1}$ becomes 3.22342 nm s$^{-1}$ under linear alignment. The opposed endpoint adjustments reduce the magnitude of the overall negative spatial slope. They do not eliminate the spatial variation: the aligned endpoints still differ by approximately 0.693 nm s$^{-1}$. Thus, temporal alignment changes the strength of the apparent trend without implying that the entire trend was an acquisition artifact.

This example was selected by the largest profile-level adjustment in O, not as a representative average. The corresponding maximum-adjustment scans in N and P are N088 and P172. Their root-mean-square changes are approximately 0.0332 and 0.1844 nm s$^{-1}$. The largest point adjustment in P172 is approximately 0.3159 nm s$^{-1}$. Selecting conspicuous examples is useful for teaching the mechanism, but quantitative conclusions about the whole record must continue to use all eligible profiles rather than only the examples that make the effect visually strong.




(a) N (b) O (c) P

**Figure 5:** Signed alignment adjustments at each retained position.

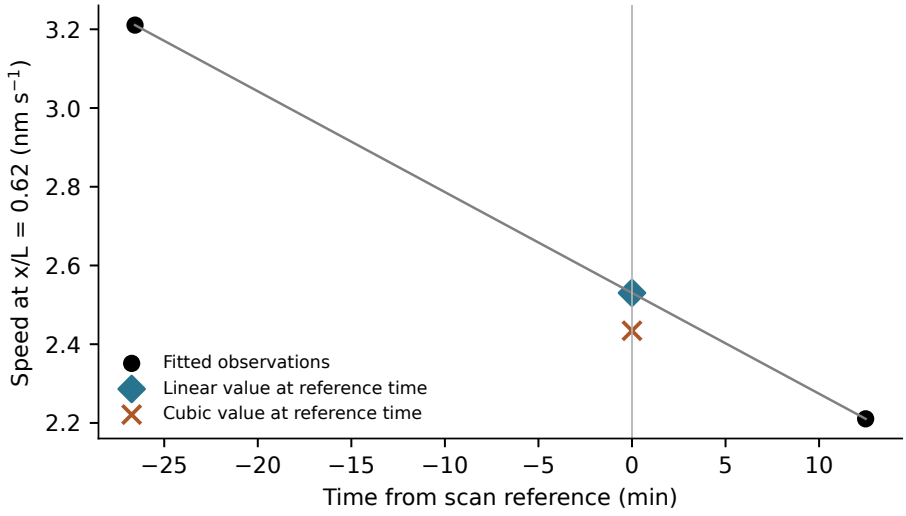



**Figure 6:** Temporal support for the O124 endpoint at normalized position 0.62.

## 4.4. Spatial slope changes do not identify motion reversal

The comparison in Figure 7 locates each retained profile by its sequential and aligned spatial slopes. Points on the identity line have unchanged slopes, while points in opposite-sign quadrants indicate a sign change. Four such cases occur in P; none occurs in N or O. The figure deliberately uses speed-gradient axes, rather than a velocity arrow, to prevent a spatial trend from being mistaken for the direction of material motion.

The four P scans are P149, P150, P170 and P171. Their sequential slopes are approximately $-1.0993$, $-0.0195$, $-0.0791$ and $0.3828$ nm s$^{-1}$ per unit $\xi$. After alignment, the values are 0.0187, 0.3607, 0.0831 and $-0.1124$. P149 illustrates a large slope reduction that ends close to zero; P150 and P170 illustrate how a shallow initial slope can change sign. These different situations should not be compressed into a single claim of a robust inversion of spatial structure.

O124 provides a complementary example because its negative slope remains negative. Alignment changes it from approximately $-3.0272$ to $-1.6660$ nm s$^{-1}$ per unit normalized position. The numerical change is substantial,

yet its interpretation is confined to the fitted spatial trend. Eq. (3) remains unchanged by the calculation. No manipulation of the time coordinate restores a sign that the underlying intensity observable does not identify.

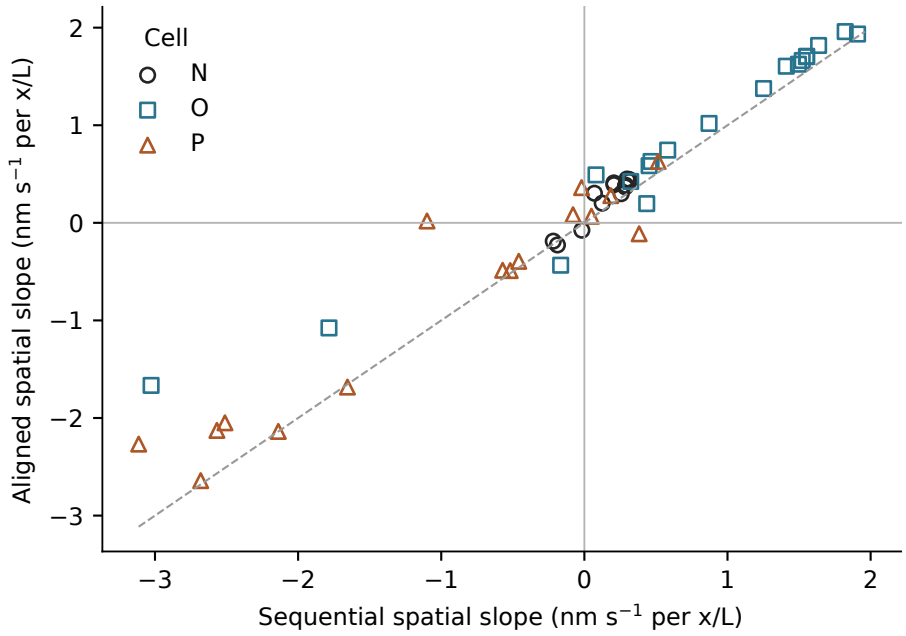



**Figure 7:** Spatial speed-gradient comparison for every eligible profile.

This separation is relevant beyond XPCS. Electrochemical transport quantities can differ when inferred through distinct measurement equations or reference frames. Studies comparing transference determinations and analyses using several operando fields show why agreement with one macroscopic response does not establish a unique microscopic interpretation [31, 32]. Here the analogous lesson is narrower: agreement of a smooth profile with an expected direction is not evidence that the measured correlation determined that direction. Numerical processing should preserve, rather than conceal, the distinction.

## 4.5. Interpolation dependence and the role of eligibility

Linear and shape-preserving cubic interpolation retain the same main set of profiles, allowing a comparison that is not confounded by changing the included scans. Median root-mean-square adjustments under the cubic treatment are 0.01328, 0.02388 and 0.04939 nm s$^{-1}$ for N, O and P. Their maxima are 0.03392, 0.19703 and 0.17165 nm s$^{-1}$. Figure 8 compares the profile-level values directly. The broadly similar scale supports the conclusion that temporal alignment matters, while departures from the identity line show that the precise adjustment is conditional on interpolation shape.

The disagreement between the two aligned estimates can be summarized separately from their disagreement with the sequential observations. Its median root-mean-square magnitude is 0.00164 nm s$^{-1}$ in N, 0.00447 in O and 0.01136 in P. The maxima are 0.00752, 0.05155 and 0.09763 nm s$^{-1}$. These values are algorithmic differences, not statistical error bars. They indicate where an interpretation that depends on a precise interpolated value should be accompanied by more frequent observations or an explicit dynamical model.

The O124 endpoint in Figure 6 illustrates the distinction. Cubic interpolation yields 2.43418 nm s$^{-1}$ at the target, approximately 0.09612 nm s$^{-1}$ below the linear estimate. Both estimates exceed the late sequential value, so the sign of the adjustment is consistent, but its magnitude is not uniquely determined by the bracketing observations. The cubic result uses neighboring trajectory shape; the linear result uses the two endpoint values alone. Neither estimator can exclude an unresolved excursion between observations.

Changing the maximum bracket interval addresses a different question. With ceilings of 0.75 or 1.0 h, the retained counts are 13, 17 and 14 for N, O and P. A ceiling of 2.0 h retains 13, 19 and 17. The associated median

adjustments are summarized in Table 3. The P median is 0.05896 nm s$^{-1}$ under either stricter rule and 0.03873 under the permissive rule. These changes arise from selection because the interpolation expression and target times are unchanged for scans retained under both rules.

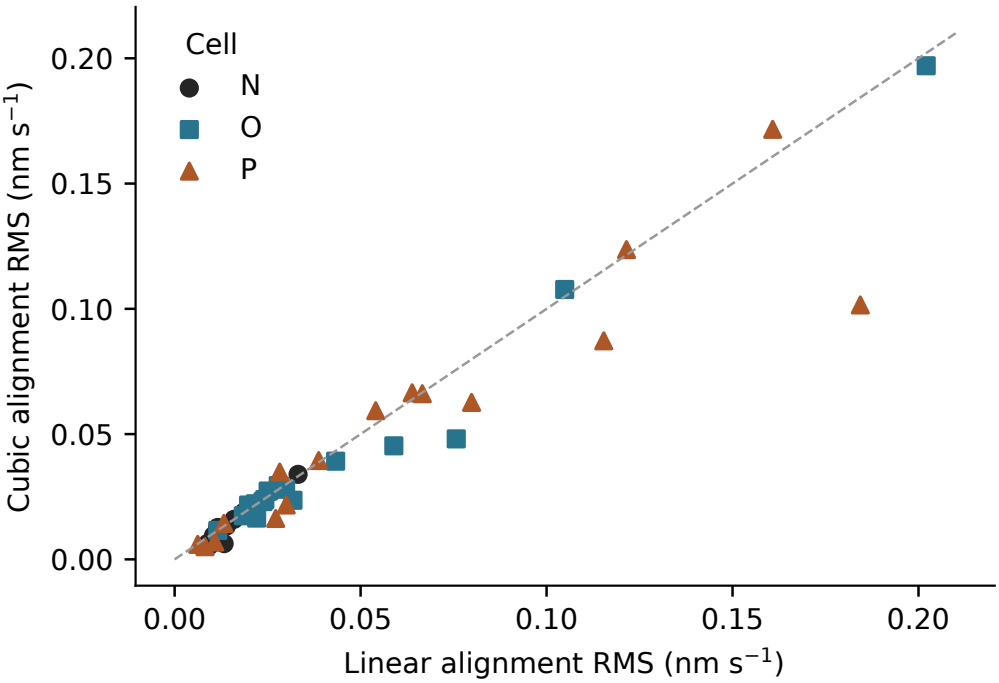



**Figure 8:** Dependence of profile-level adjustment on interpolation shape.

Figure 4 expresses the included counts relative to the number of complete profiles. N is unaffected over the tested range; O gains profiles between the stricter and main settings; P changes at both ends. The main retained profiles have median maximum brackets of approximately 0.651 h, with maxima of 0.652, 1.301 and 1.302 h. Thus, some estimates use a longer-than-usual return interval. The interval ceiling is scientifically meaningful as a support requirement even though it should not be interpreted as a physical boundary between reliable and unreliable material behavior.

**Table 3:** Effect of the temporal bracket ceiling. Each cell entry gives retained count followed by median linear RMS adjustment in nm s$^{-1}$.

| Ceiling (h) | N: count; median | O: count; median | P: count; median |
|---|---|---|---|
| 0.75 | 13; 0.01394 | 17; 0.02514 | 14; 0.05896 |
| 1.00 | 13; 0.01394 | 17; 0.02514 | 14; 0.05896 |
| 1.50 | 13; 0.01394 | 19; 0.02514 | 16; 0.04640 |
| 2.00 | 13; 0.01394 | 19; 0.02514 | 17; 0.03873 |

The electrical-clearance check removes one O profile and none from N or P. The O median adjustment becomes 0.02470 nm s$^{-1}$, compared with 0.02514 in the main calculation. This modest change indicates that the median does not depend strongly on the single excluded profile. It does not prove stationarity during every remaining acquisition. A clearance around known electrical changes tests one identifiable source of concern; structural relaxation, interfacial evolution and instrumental drift may continue away from those boundaries.

The interpolation assumptions can also be expressed as a conditional mathematical bound. If a twice differentiable speed trajectory has a second derivative whose magnitude does not exceed $M$ throughout a bracket, the linear interpolation error at an interior target satisfies

$$|u(t^{*}) - \widehat{u}(t^{*})| \le \frac{M}{2}(t^{*} - t_{a})(t_{b} - t^{*}) \le \frac{M}{8}(t_{b} - t_{a})^{2}. \tag{9}$$

The bound follows from the remainder of the linear interpolating polynomial. Its quadratic dependence on bracket duration explains why controlling the revisit interval is physically relevant. It does not supply an error bar here because the observations do not establish a defensible upper bound on the unobserved temporal curvature. Estimating curvature from a few noisy fitted values and treating that estimate as a guaranteed bound would replace one unsupported assumption with another.

This distinction helps interpret the comparison between linear and cubic estimates. Their agreement is reassuring only within the range of temporal shapes admitted by those methods. Both can miss an excursion that begins and ends between consecutive observations. A small difference between the methods therefore cannot prove that the simultaneous field is known accurately. Conversely, a larger difference identifies dependence on local trajectory shape without proving that either estimate is incorrect. The useful scientific conclusion concerns sensitivity to assumptions, not selection of an algorithm by its visual smoothness.

The same reasoning clarifies why the interval restriction and electrical clearance are complementary. A short bracket may still cross a polarity reversal, where smooth continuation of a trajectory is particularly questionable. A bracket entirely within one electrical phase can nevertheless be too long to support a rapidly changing response. Requiring both conditions constrains two distinct aspects of the estimate. The additional clearance removes observations close to a transition but does not establish that the remaining trajectory has small curvature. Each check must retain its own limited interpretation.

An experimental response to these limitations would place repeat observations where the trajectory changes fastest, provided the material tolerates the associated exposure. Such adaptive sampling would require a rule established before evaluating the resulting spatial contrast. Otherwise, the schedule could preferentially retain interesting periods and change the meaning of aggregate summaries. For the present records, no adaptive acquisition is claimed. The value of the bound is instructional: it links a temporal sampling decision to a mathematical assumption and makes explicit which unmeasured quantity prevents a rigorous numerical accuracy statement. This reasoning is more informative than assigning an arbitrary percentage uncertainty to every aligned point, because the possible interpolation error depends on both temporal curvature and the actual location of the target within its bracket.

A related caution concerns numerical precision. Keeping many digits in the calculated target time is useful for reproducing the arithmetic, but it does not imply equally precise instrument synchronization. Likewise, rounding the displayed speed adjustment to three decimals does not identify a physical detection limit. The figures and tables use sufficient precision to distinguish the calculations while the interpretation remains tied to the recorded timing and the availability of supporting observations at each position throughout the acquisition.

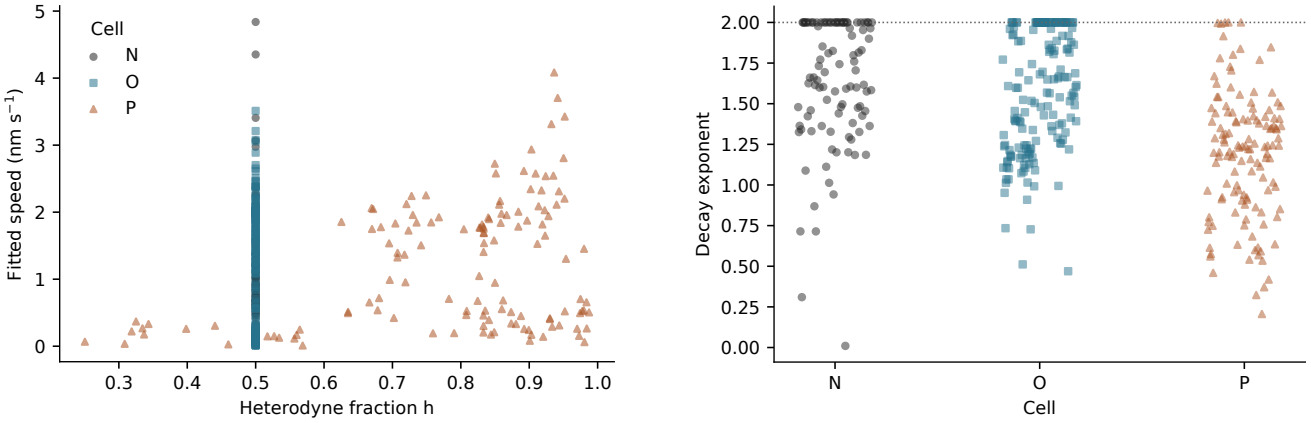
## 4.6. Fit parameters and spatial registration constrain interpretation

Figure 9 examines two quantities retained with the speed estimates. The heterodyne fraction is fixed at 0.5 throughout the finite N and O records. In P, it ranges from 0.25032 to 0.98745, with a median of 0.84010. These differences are important because the fraction controls the relative contribution of reference and dynamic scattering in the fit. Comparing speed distributions across cells without acknowledging this distinction would combine quantities estimated under different parameter constraints.

The decay exponent also warrants attention. Values at or above 1.9999 occur in 32 N records, 43 O records and three P records. This proximity to a common numerical value is compatible with a constrained fitting treatment, but the table alone does not establish the optimizer settings or explain each occurrence. The figure therefore shows the actual values without labeling them failed fits. Parameter residuals, covariance, convergence records and sensitivity to alternative starting values would be needed to distinguish a physical concentration near that exponent from a boundary-related numerical effect.

No exclusion is introduced solely because of these parameter patterns. Removing observations according to an undocumented quality threshold would add another selection mechanism without a validated criterion. Instead, the patterns delimit the cross-cell interpretation and identify information needed for a detector-level assessment.

Software for interactive XPCS analysis supports inspection of scattering patterns, correlations and measurement stability [33]; those richer checks cannot be reconstructed from fitted speed and parameter columns alone.




(a) Heterodyne fraction and speed

(b) Decay-exponent values

**Figure 9:** Variation in quantities accompanying the fitted speeds. The fixed heterodyne fraction in N and O differs from the variable fraction in P. The dotted exponent line marks 1.9999, used only to count values near two.

Motor coordinates provide another qualification. At a fixed nominal position, the horizontal coordinate spans 0.080 in the stored units for N, 0.160 for O and 0.120 for P. Within a scan, successive nominal positions remain spaced by approximately 0.300 in that coordinate. These shifts show that the nominal label is not identical to an unchanged absolute motor setting throughout the experiment. The records examined here do not independently determine whether the shifts preserve electrode-relative registration, deliberately move the illuminated region, or reflect another acquisition adjustment.

Temporal interpolation is consequently conditional on comparable nominal positions. It should not be described as tracking exactly the same material volume unless registration is separately verified. A moving beam can change both the time and the sampled volume. Conversely, a changed motor coordinate may preserve a relative position if the sample reference also moves. The numerical record cannot choose between these possibilities without geometric calibration, so the analysis retains the documented normalized labels and treats unverified registration as a physical limitation.

## 4.7. Radiation effects and evolving material states

Changes in fitted dynamics can have more than one origin. X-ray illumination can itself induce motion in oxide glasses, while measurements of protein gels have distinguished driven and intrinsic dynamical contributions [34, 35]. These are different materials from the electrolyte considered here, and their quantitative responses are not transferred to SEO. Their methodological relevance is that a temporal change in a coherent-scattering signal need not be caused solely by the externally applied electrical protocol.

Low-dose speckle-visibility measurements illustrate an alternative approach to radiation-sensitive soft matter [36]. Improvements in coherent flux and ultra-small-angle XPCS likewise extend measurement capability while making acquisition choices increasingly consequential [37]. More photons can improve precision, but exposure, illuminated volume and sample renewal still enter the physical interpretation. The fitted records used in the present calculation do not supply sufficient dose information to separate an illumination-induced change from the electrochemical response.

The same caution applies to structural evolution. Operando characterization of organic mixed ionic/electronic conductors emphasizes concurrent changes in composition and morphology, and time-resolved XPCS has connected electrochemical actuation with mesoscale strain and dynamics [38, 39]. These systems are not interchangeable with a block copolymer electrolyte. They demonstrate why a physical description of what scatters and how the material

is driven must accompany any temporal processing. Aligning timestamps cannot determine whether a changing speed reflects translation, changing contrast or a limitation of the fitted model.

The numerical findings should therefore be stated at their actual level of support. An acquisition order extending over twenty-five minutes is not negligible merely because the fit values appear precise. Temporal alignment changes several spatial comparisons, and some changes depend on interpolation. However, the calculation does not establish a new ion-transport mechanism, a new material phase or an instrumental accuracy. It identifies how the interpretation of existing fitted measurements depends on acquisition history, which is the appropriate scientific content for this study.

## 5. TEACHING THE MEASUREMENT-TO-INTERPRETATION CHAIN

The teaching sequence begins with the observable, rather than with software commands. Readers first expand the coherent intensity in Eq. (1) and identify which term connects the moving and stationary contributions. They then apply the sign transformation in Eq. (3). The expected written conclusion is precise: an even intensity-correlation term does not determine the sign of projected translation. A response that assigns direction from electrical polarity alone must identify the additional physical assumption. This exercise separates a mathematical limitation from random experimental uncertainty before numerical processing begins.

A second exercise concerns units and the two clocks. Readers convert angstroms per second to nanometers per second and reconstruct elapsed electrical time for one cell using Eq. (4). The required evidence is a worked substitution, not only a correctly labeled graph. A factor-of-ten speed error changes every later adjustment, while an origin error can place observations in the wrong electrical phase. The two mistakes may still produce smooth plots. Their detection requires explicit numerical checks rather than visual confidence in the final curve.

The acquisition-accounting exercise follows. Learners distinguish a measurement row, a scan prefix, a complete five-position profile and a profile with admissible temporal support. They must recover the total finite count and explain why attempted prefixes and prefixes with finite values differ. This distinction provides a concrete encounter with missingness: an absent fitted value is not zero motion, and a complete spatial curve can still lack valid bracketing observations. Correct reasoning about the denominator is assessed independently of the interpolation arithmetic.

The central numerical exercise reconstructs the endpoint estimate in Figure 6. Learners identify the two actual observations surrounding the reference time, calculate the linear weight and recover the aligned speed. They compare that value with the sequential observation and state which is measured and which is estimated. They then inspect the cubic result. Agreement in the sign of the adjustment, accompanied by a difference in magnitude, provides a direct basis for discussing interpolation assumptions without claiming that one algorithm has discovered the true instantaneous state.

Spatial reasoning is assessed through Figure 7. Learners explain why an off-identity point need not imply an incorrect fit and why an opposite-sign quadrant does not imply motion reversal. A stronger answer also identifies the limitation of compressing a curved profile into one slope. The shallow-slope examples in P are useful because the sign changes are numerically real yet do not all represent large spatial reorganizations. This encourages attention to scale and definition before categorical language is applied.

A further exercise holds the interpolation formula fixed while changing the interval ceiling. Learners explain why the median can change when the estimates for common retained scans do not. The task distinguishes selection effects from algorithmic effects. It can be completed by comparing scan identities across the stricter and permissive settings, rather than by relying on a verbal explanation alone. The appropriate conclusion concerns which observations support the calculation, not whether a particular ceiling has been proven universally optimal.

Contemporary computational tools provide a useful extension, provided their input requirements remain clear. Neural-network denoising can improve correlation images, while learned representations can classify non-equilibrium relaxation behavior [40, 41]. Reverse-engineering approaches can relate two-time structures to candidate microscopic processes [42]. These methods operate on information richer than a table of fitted speeds. Introducing them after

the worked examples helps learners understand why computational sophistication cannot recover a missing detector record or resolve a directional symmetry without additional information.

The final exercise asks readers to design an acquisition that would reduce the ambiguity exposed here. Alternating spatial order, revisiting a reference position or shortening the observation sequence are defensible possibilities. Each proposal must specify the uncertainty it addresses and the cost it introduces. Shorter acquisitions may reduce temporal averaging while weakening correlation precision; additional reference visits consume time; changing the illuminated region may limit exposure but complicate spatial registration. The task is not to select a universally best arrangement, but to justify a measurement decision in relation to a stated physical question.

These activities constitute an instructional design with explicit answer criteria. They are not evidence that the instruction improves learning. No students were enrolled, no assessment scores were collected and no comparison of teaching approaches was performed. An educational evaluation would require a defined participant population, scoring rules and an appropriate study design. Maintaining this distinction allows the article to make a useful contribution as a technical study without assigning an educational effect to untested classroom activities.

## 6. MEASUREMENT REQUIREMENTS FOR STRONGER PHYSICAL CONCLUSIONS

The most valuable additional records would be the scattering intensities and correlation functions associated with each fitted point. They would permit examination of oscillation visibility, decorrelation form, contrast evolution and residual structure. Two-time analysis could test whether the dynamics remain stationary within an observation window. A model that produces one plausible fitted speed may not explain evolving correlations equally well. Without these records, the present alignment calculation must treat the fitted quantities as inputs whose upstream validity remains conditional.

Fit uncertainty should also be retained with the full parameter dependence. A speed interval estimated while fixing the heterodyne fraction is different from one obtained when that fraction is freely adjusted. Correlations among speed, decay time, exponent and contrast can influence identifiability even when the directional ambiguity is already understood. Reporting separate standard deviations without their covariance may still conceal compensation between parameters. These considerations explain why the algorithmic differences examined here cannot be relabeled as confidence intervals for the material velocity.

Timing records should specify the acquisition reference convention, window duration and any averaging applied before fitting. A common timestamp offset makes the numerical clocks comparable but does not certify their synchronization. If the detector and potentiostat clocks drift relative to each other, a constant offset can become inadequate. If the timestamp denotes the end of acquisition rather than its midpoint, interpreting it as an instantaneous observation shifts the represented interval. The appropriate correction requires instrument documentation, not a convenient assumption selected to improve agreement.

Spatial records should connect motor settings to electrode-relative coordinates and document any change in illuminated volume. The observed coordinate shifts make this requirement concrete. A statement that nominal position three corresponds to one normalized location is useful, but it does not independently prove that repeated visits interrogate the same material volume. Beam dimensions, sample motion, electrode geometry and reference-compartment alignment enter that determination. Verification would strengthen temporal interpolation by establishing that it compares observations whose spatial meaning is also controlled.

Independent physical conclusions would further require repeated cells prepared under a defined protocol. Additional times within one cell improve temporal coverage but do not substitute for independent preparation. A comparison of cell behavior should specify which factors are matched, including material composition, electrode condition, temperature history and fit treatment. The present three series are sufficient to illustrate the timing problem in several operating records; they do not establish the variance of a material property across a manufacturing or preparation population.

# 7. CONCLUSIONS

Operando heterodyne XPCS requires two distinctions to remain explicit: intensity correlations identify a projected speed magnitude under the adopted fit, and sequential spatial visits represent different observation times. In the three polymer-electrolyte series examined here, a five-position profile spans approximately twenty-five minutes between stored timestamps. A phase-preserving linear calculation retains 48 complete profiles and changes their spatial comparison by amounts that vary strongly across the record. The largest point adjustment is approximately 0.320 $\mathrm{nm\,s^{-1}}$, while four P profiles change the sign of their fitted speed gradient.

Alternative interpolation preserves the overall scale of temporal sensitivity but changes some individual estimates. Interval restrictions alter profile inclusion, and electrical-clearance checks test only proximity to known transitions. Fit-parameter differences and unverified physical registration impose additional limits. These findings support a study centered on the actual observable and acquisition history, rather than a claim of a uniquely recovered instantaneous field.

The educational outcome sought is an interpretable scientific statement: what was measured, what was estimated, and which physical conclusion follows under stated assumptions. Maintaining those distinctions permits the numerical analysis to inform materials characterization without converting fitted magnitudes into signed motion, repeated observations into independent specimens, or proposed learning activities into demonstrated educational effects.

## Conflict of Interests

The author declares that they have no conflicts of interest.

## Funding Information

This research received no external funding.

## Data Availability

The data supporting the findings of this study are available from the author upon reasonable request.

## References

1. Y. Choo, D. M. Halat, I. Villaluenga, K. Timachova, N. P. Balsara, Diffusion and migration in polymer electrolytes, *Progress in Polymer Science* **103** (2020) 101220, 10.1016/j.progpolymsci.2020.101220.
2. Y. Kambe, C. G. Arges, D. A. Czaplewski, M. Dolejsi, S. Krishnan, M. P. Stoykovich, et al., Role of Defects in Ion Transport in Block Copolymer Electrolytes, *Nano Lett.* **19** (2019) 4684-4691, 10.1021/acs.nanolett.9b01758.
3. M. D. Galluzzo, W. S. Loo, A. A. Wang, A. Walton, J. A. Maslyn, N. P. Balsara, Measurement of Three Transport Coefficients and the Thermodynamic Factor in Block Copolymer Electrolytes with Different Morphologies, *J. Phys. Chem. B* **124** (2020) 921-935, 10.1021/acs.jpcb.9b11066.
4. W. S. Loo, M. D. Galluzzo, X. Li, J. A. Maslyn, H. J. Oh, K. I. Mongcopa, et al., Phase Behavior of Mixtures of Block Copolymers and a Lithium Salt, *J. Phys. Chem. B* **122** (2018) 8065-8074, 10.1021/acs.jpcb.8b04189.
5. M. D. Galluzzo, W. S. Loo, E. Schaible, C. Zhu, N. P. Balsara, Dynamic Structure and Phase Behavior of a Block Copolymer Electrolyte under dc Polarization, *ACS Appl. Mater. Interfaces* **12** (2020) 57421-57430, 10.1021/acsami.0c16209.
6. M. D. Galluzzo, L. S. Grundy, C. J. Takacs, C. Cao, H. G. Steinrück, S. Fu, et al., Orientation-Dependent Distortion of Lamellae in a Block Copolymer Electrolyte under DC Polarization, *Macromolecules* **54** (2021) 7808-7821, 10.1021/acs.macromol.1c01295.
7. J. A. Maslyn, L. Frenck, V. D. Veeraraghavan, A. Müller, A. S. Ho, N. Marwaha, et al., Limiting Current in Nanostructured Block Copolymer Electrolytes, *Macromolecules* **54** (2021) 4010-4022, 10.1021/acs.macromol.1c00425.
8. L. S. Grundy, M. D. Galluzzo, W. S. Loo, A. Y. Fong, N. P. Balsara, C. J. Takacs, Inaccessible Polarization-Induced Phase Transitions in a Block Copolymer Electrolyte: An Unconventional Mechanism for the Limiting

Current, *Macromolecules* **55** (2022) 7637-7649, 10.1021/acs.macromol.2c00922.
9. I. Villaluenga, D. M. Pesko, K. Timachova, Z. Feng, J. Newman, V. Srinivasan, et al., Negative Stefan-Maxwell Diffusion Coefficients and Complete Electrochemical Transport Characterization of Homopolymer and Block Copolymer Electrolytes, *J. Electrochem. Soc.* **165** (2018) A2766-A2773, 10.1149/2.0641811jes.
10. Y. Shao, H. Gudla, D. Brandell, C. Zhang, Transference Number in Polymer Electrolytes: Mind the Reference-Frame Gap, *J. Am. Chem. Soc.* **144** (2022) 7583-7587, 10.1021/jacs.2c02389.
11. A. Mistry, L. S. Grundy, D. M. Halat, J. Newman, N. P. Balsara, V. Srinivasan, Effect of Solvent Motion on Ion Transport in Electrolytes, *J. Electrochem. Soc.* **169** (2022) 040524, 10.1149/1945-7111/ac6329.
12. D. M. Halat, A. Mistry, D. Hickson, V. Srinivasan, N. P. Balsara, J. A. Reimer, Transference Number of Electrolytes from the Velocity of a Single Species Measured by Electrophoretic NMR, *J. Electrochem. Soc.* **170** (2023) 030535, 10.1149/1945-7111/acbee7.
13. M. Lorenz, F. Kilchert, P. Nürnberg, M. Schammer, A. Latz, B. Horstmann, et al., Local Volume Conservation in Concentrated Electrolytes Is Governing Charge Transport in Electric Fields, *J. Phys. Chem. Lett.* **13** (2022) 8761-8767, 10.1021/acs.jpclett.2c02398.
14. A. Mistry, V. Srinivasan, H. Steinrück, Characterizing Ion Transport in Electrolytes via Concentration and Velocity Profiles, *Advanced Energy Materials* **13** (2023) 2203690, 10.1002/aenm.202203690.
15. H. G. Steinrück, C. J. Takacs, H. K. Kim, D. G. Mackanic, B. Holladay, C. Cao, et al., Concentration and velocity profiles in a polymeric lithium-ion battery electrolyte, *Energy Environ. Sci.* **13** (2020) 4312-4321, 10.1039/d0ee02193h.
16. M. D. Galluzzo, H. G. Steinrück, C. J. Takacs, A. Mistry, L. S. Grundy, C. Cao, et al., Probing transference and field-induced polymer velocity in block copolymer electrolytes, *Cell Reports Physical Science* **5** (2024) 101766, 10.1016/j.xcrp.2023.101766.
17. J. R. M. Lhermitte, M. C. Rogers, S. Manet, M. Sutton, Velocity measurement by coherent x-ray heterodyning, *Review of Scientific Instruments* **88** (2017) 015112, 10.1063/1.4974099.
18. H. Li, M. Ladd-Parada, A. Karina, F. Dallari, M. Reiser, F. Perakis, et al., Intrinsic Dynamics of Amorphous Ice Revealed by a Heterodyne Signal in X-ray Photon Correlation Spectroscopy Experiments, *J. Phys. Chem. Lett.* **14** (2023) 10999-11007, 10.1021/acs.jpclett.3c02470.
19. A. R. Sandy, Q. Zhang, L. B. Lurio, Hard X-Ray Photon Correlation Spectroscopy Methods for Materials Studies, *Annu. Rev. Mater. Res.* **48** (2018) 167-190, 10.1146/annurev-matsci-070317-124334.
20. G. Stoclet, D. Schwaller, R. Garlet, F. Livet, G. A. Chahine, N. Blanc, et al., Structural dependency of polymer dynamics by means of small-angle X-ray photon correlation spectroscopy and wide-angle X-ray scattering on the D2AM beamline, *J Synchrotron Rad* **32** (2025) 649-660, 10.1107/s1600577525001626.
21. O. Bikondoa, On the use of two-time correlation functions for X-ray photon correlation spectroscopy data analysis, *J Appl Crystallogr* **50** (2017) 357-368, 10.1107/s1600576717000577.
22. A. Ragulskaya, V. Starostin, F. Zhang, C. Gutt, F. Schreiber, On the analysis of two-time correlation functions: equilibrium versus non-equilibrium systems, *J Appl Crystallogr* **57** (2024) 1098-1106, 10.1107/s1600576724004618.
23. H. G. Steinrück, General relationship between salt concentration and x-ray absorption for binary electrolytes, *AIP Advances* **11** (2021) 115119, 10.1063/5.0072947.
24. O. M. Magnussen, J. Drnec, C. Qiu, I. Martens, J. J. Huang, R. Chattot, et al., In Situ and Operando X-ray Scattering Methods in Electrochemistry and Electrocatalysis, *Chem. Rev.* **124** (2024) 629-721, 10.1021/acs.chemrev.3c00331.
25. Q. Zhang, E. M. Dufresne, Y. Nakaye, P. R. Jemian, T. Sakumura, Y. Sakuma, et al., 20 $\mu$s-resolved high-throughput X-ray photon correlation spectroscopy on a 500k pixel detector enabled by data-management workflow, *J Synchrotron Rad* **28** (2021) 259-265, 10.1107/s1600577520014319.
26. S. Berkowicz, S. Das, M. Reiser, M. Filianina, M. Bin, G. Crevatin, et al., Nanofocused x-ray photon correlation spectroscopy, *Phys. Rev. Research* **4** (2022) L032012, 10.1103/physrevresearch.4.l032012.
27. F. Lehmkühler, F. Dallari, A. Jain, M. Sikorski, J. Möller, L. Frenzel, et al., Emergence of anomalous dynamics in soft matter probed at the European XFEL, *Proc. Natl. Acad. Sci. U.S.A.* **117** (2020) 24110-24116, 10.1073/pnas.2003337117.

28. F. Perakis, C. Gutt, Towards molecular movies with X-ray photon correlation spectroscopy, *Phys. Chem. Chem. Phys.* **22** (2020) 19443-19453, 10.1039/d0cp03551c.
29. F. Lehmkühler, W. Roseker, G. Grübel, From Femtoseconds to Hours—Measuring Dynamics over 18 Orders of Magnitude with Coherent X-rays, *Applied Sciences* **11** (2021) 6179, 10.3390/app11136179.
30. M. Galluzzo, Supplemental Data for Cell Reports Physical Science article "Probing transference and field-induced polymer velocity in block copolymer electrolytes", Zenodo, v1 (2023), 10.5281/zenodo.10251535.
31. D. T. Hickson, N. Balsara, Toward Establishing Uniqueness of Experimentally Determined Transference Numbers, *J. Electrochem. Soc.* **172** (2025) 040528, 10.1149/1945-7111/adca04.
32. A. Mistry, H. G. Steinrück, M. F. Toney, N. P. Balsara, V. Srinivasan, Multiple Operando Fields Can Identify a Predictive Mass Transport Theory in Electrolytes, *J. Phys. Chem. C* **129** (2025) 2874-2882, 10.1021/acs.jpcc.4c06851.
33. M. Chu, J. Li, Q. Zhang, Z. Jiang, E. M. Dufresne, A. Sandy, et al., pyXPCSviewer : an open-source interactive tool for X-ray photon correlation spectroscopy visualization and analysis, *J Synchrotron Rad* **29** (2022) 1122-1129, 10.1107/s1600577522004830.
34. B. Ruta, F. Zontone, Y. Chushkin, G. Baldi, G. Pintori, G. Monaco, et al., Hard X-rays as pump and probe of atomic motion in oxide glasses, *Sci Rep* **7** (2017) 3962, 10.1038/s41598-017-04271-x.
35. S. Timmermann, N. D. Anthuparambil, A. Girelli, N. Begam, M. Kowalski, S. Retzbach, et al., X-ray driven and intrinsic dynamics in protein gels, *Sci Rep* **13** (2023) 11048, 10.1038/s41598-023-38059-z.
36. J. Möller, M. Reiser, J. Hallmann, U. Boesenberg, A. Zozulya, H. Rahmann, et al., Using low dose x-ray speckle visibility spectroscopy to study dynamics of soft matter samples, *New J. Phys.* **23** (2021) 093041, 10.1088/1367-2630/ac2594.
37. W. Chèvremont, T. Zinn, T. Narayanan, Improvement of ultra-small-angle XPCS with the Extremely Brilliant Source, *J Synchrotron Rad* **31** (2024) 65-76, 10.1107/s1600577523008627.
38. R. Wu, M. Matta, B. D. Paulsen, J. Rivnay, Operando Characterization of Organic Mixed Ionic/Electronic Conducting Materials, *Chem. Rev.* **122** (2022) 4493-4551, 10.1021/acs.chemrev.1c00597.
39. R. Wu, D. Meli, J. Strzalka, S. Narayanan, Q. Zhang, B. D. Paulsen, et al., Bridging length scales in organic mixed ionic–electronic conductors through internal strain and mesoscale dynamics, *Nat. Mater.* **23** (2024) 648-655, 10.1038/s41563-024-01813-3.
40. T. Konstantinova, L. Wiegart, M. Rakitin, A. M. DeGennaro, A. M. Barbour, Noise reduction in X-ray photon correlation spectroscopy with convolutional neural networks encoder–decoder models, *Sci Rep* **11** (2021) 14756, 10.1038/s41598-021-93747-y.
41. J. P. Horwath, X. M. Lin, H. He, Q. Zhang, E. M. Dufresne, M. Chu, et al., AI-NERD: Elucidation of relaxation dynamics beyond equilibrium through AI-informed X-ray photon correlation spectroscopy, *Nat Commun* **15** (2024) 5945, 10.1038/s41467-024-49381-z.
42. A. Ragulskaya, V. Starostin, N. Begam, A. Girelli, H. Rahmann, M. Reiser, et al., Reverse-engineering method for XPCS studies of non-equilibrium dynamics, *IUCrJ* **9** (2022) 439-448, 10.1107/s2052252522004560.